IEEE Access
Multidisciplinary | Rapid Review | Open Access Journal

Received July 23, 2020, accepted July 31, 2020, date of publication August 4, 2020, date of current version August 18, 2020.

Digital Object Identifier 10.1109/ACCESS.2020.3014170

Three-Dimensional Terahertz Continuous Wave Imaging Radar for Nondestructive Testing

XIAOXUAN ZHANG[1], TIANYING CHANG[1,2], ZHONGMIN WANG[1], AND HONG-LIANG CUI[1,3]

[1]College of Instrumentation and Electrical Engineering, Jilin University, Changchun 130012, China
[2]Institute of Automation, Qilu University of Technology (Shandong Academy of Sciences), Jinan 250014, China
[3]Chongqing Institute of Green and Intelligent Technology, Chinese Academy of Sciences, Chongqing 400714, China

Corresponding author: Tianying Chang (tchang@jlu.edu.cn)

This work was supported in part by the National Natural Science Foundation of China under Grant 61875196 and Grant 61705120, and in part by the Major Scientific and Technological Innovation Projects of Shandong Province under Grant 2019JZZY010448.

ABSTRACT In recent years, our research group has been devoting substantial efforts to the research and development of active all-solid-state electronic terahertz (THz) continuous wave imaging systems for nondestructive testing, which is currently benefitting from the increasing amount of transmitting power, high performance/cost ratio and adaptability to engineering. In this paper, an in-house developed broadband linear frequency modulated continuous wave (LFMCW) three-dimensional (3D) THz imaging system is described, and two sets of experimental platforms are set up to assist the planning and completion of the research, including a narrow-band LFMCW 3D imaging radar and a wide-band stepped-frequency modulated continuous wave 3D imaging radar. For 3D imaging systems, to cope with demanding scenarios and to achieve excellent imaging performance, various reconstruction algorithms are explored. The first is a spectral refinement and correction approach based on fast Fourier transform and modern spectral estimation for accurate thickness measurement. The second is the synthetic aperture radar imaging algorithm for surface detection or internal detection of objects with lower refractive index. The third is a 3D reconstruction algorithm based on half space Green's function and the exploding source model for the interior detection of materials with higher refractive index. The fourth is the frequency interference algorithm combining phase unwrapping to measure uneven and nonplanar surfaces. Exploiting these systems, along with the associated experimental platforms and reconstruction algorithms, we successfully implemented non-destructive testing for objects with various defects and of different materials, such as polymer boards with voids, and foam with inclusions.

INDEX TERMS Continuous wave imaging sensors, nondestructive testing, three-dimensional reconstruction, all-solid-state electronics.

I. INTRODUCTION

Nondestructive testing technology plays an important role in ensuring product quality and providing early warning against operation failure. Common detection methods have their own application occasions and limitations, such as ultrasonic detection, infrared thermal image, and laser holography [1]–[3]. Thanks to the development of semiconductor technology and ultrafast optoelectronics, terahertz electromagnetic radiation has attracted much attention since the mid-1980s [4], which is located between the microwave and infrared regions of the electromagnetic spectrum [5], [6]. One of the most important applications of electromagnetic waves is imaging [7]. Like other frequency ranges, THz wave can also be used in imaging and offers several unique advantages. Compared with microwave, it is superior in terms of image resolution due to its shorter wavelength and wider tuning band [8]. Compared with high-energy photons such as X-rays, it is intrinsically safe due to its low photon energy, rendering it nonionizing, and there is no apprehension on human health if appropriate transmitted power level is chosen [9], [10]. Besides, compared with the visible or infrared band, THz wave has a higher transmittance in nonmetallic and nonpolar materials. Also, unlike ultrasound

The associate editor coordinating the review of this manuscript and approving it for publication was Xiaokang Yin.

imaging, it does not need messy couplant and can offer better spatial resolution. Thus THz imaging can be a useful complementary and beneficial addition to the traditional nondestructive testing (NDT) repertoire [11], [12].

Terahertz imaging was first proposed based on femtosecond laser and photoelectric sampling technology in the late 1970's, which belongs to pulse imaging technology [1]. However, the development and application of terahertz pulse imaging systems are restricted by the demand on the pump laser, including transmitting power, operating environment, integration and cost [13], [14]. Typically femtosecond laser, free electron laser, quantum cascade laser, CO_2-pumped laser and fiber laser were used [15]. Among them, fiber laser is the most widely used because of its small size, high energy conversion efficiency, and suitability for portable systems. However, these systems are still several times larger and more expensive than the all-solid-state terahertz continuous wave imaging system, and require constant-temperature and humidity working environment, which are best placed in ultra-clean chamber. Secondly, the delay line, an indispensable part of the THz time-domain spectroscopic system, is usually controlled by mechanical linear or rotary motion, which directly impact on the time and frequency resolution, and it limits the scanning time and the image reconstruction rate. In recent years, some research groups have developed non-mechanical scanning delayers with dual-pulse lasers of different frequencies, but at the cost of adding an expensive femtosecond laser and electronic feedback, which increases the cost and complexity [15]–[17]. Thirdly, the maximum thickness of measurable sample is about 10 mm, limited by the length of the delay line. And taking into account the transmission loss and focal length limitation, the maximum thickness that can be measured will get smaller. In addition, the emission power is low, generally below 100 nanowatt, such as the terahertz time-domain spectral (THz-TDS) system of Zomega's FiCO model [18]. Therefore, THz-TDS system is mainly suitable for detecting thin samples. Given the above limitations, portable active all-solid-state electronic THz CW imaging system is currently a research hotspot, which can be applied to security inspection [19], non-destructive testing [11] and 5G or 6G wireless communications [20]. Compared with the passive mode, active imaging is of high spatial resolution, good signal-to-noise ratio (SNR), and capable of three-dimensional (3D) imaging with broadband sources [21], [22]. Moreover, the solid-state electronic structure is more compact and noise-resistant, easy to modularize and/or integrate, than the optical structure, making it more suitable for engineering applications.

In recent years, many groups have carried out research on solid-state electronic THz CW imaging radars. Here are some leading research results. NASA Jet Propulsion Laboratory (JPL) was the first institution to invest in CW terahertz imaging and has exerted a profound influence in this field. So far, several high-performance THz imaging systems have been developed based on THz frequency modulated continuous wave (FMCW), which are mainly used for space exploration and security inspection [19], [23]–[25]. Among them, the two imaging systems with frequency ranges of 576∼604.8 GHz and 662.4∼691.2 GHz have the widest bandwidth of nearly 30 GHz [24], [19]. Recently, JPL is leveraging FMCW technology for planetary and earth science applications [26]. For the problem of measuring the 0.1-10 mm scale particle distributions and dynamics in jets occurring on comets and icy moons in the solar system, a 95 GHz FMCW Doppler radar is being developed for detecting both volumetric and single-particle scattering. Also being developed is a 183 GHz differential radar transceiver for humidity sounding within high altitude ice clouds on earth. Another representative laboratory that is active in THz radar imaging in the US is the Pacific Northwest National Laboratory (PNNL), which launched the security screening project of terahertz imaging systems based on FMCW [27], [28]; Apparently range resolution is not an overriding concern here and the widest bandwidth is only 19.2 GHz. In recent years, the PNNL team has been mainly engaged in the research of millimeter wave (mmW) and terahertz wave imaging for security inspection with novel near-field sparse multi-static array structure and reconstruction algorithms, rather than the development of the hardware system [29], [30]. In Europe, Fraunhofer Institute for High Frequency Physics and Radar Techniques (FHR) in Germany first carried out works in this field and has designed several systems for imaging of human bodies and vehicles, in which the widest bandwidth is 44 GHz [31]–[33]. The German firm SynView launched a FMCW system named SynView Head-300, which is of the most wide-band (up to 90 GHz), which has been successfully applied in thickness measurement and nondestructive testing by some research groups, such as Fraunhofer Institute for Physical Measurement Techniques and Huazhong University of Science and Technology in China [11], [34], [35]. These teams have studied effective image processing methods, such as image segmentation and edge extraction, but the electromagnetic reconstruction algorithm still follows the common synthetic aperture radar (SAR) algorithm, such as the range migration algorithm (RMA) [11], [36]. In addition, countries such as Sweden [37], Israel [38], the UK [39], Spain [40] and China [12] have also conducted research on THz FMCW imaging radar. Most of the terahertz FMCW systems mentioned above focus on security inspection at mass-transportation stations, airports and custom check points [41], or air-to-air and air-to-ground military activities and few are designed for non-destructive testing, which require somewhat different and perhaps more nuanced technical consideration.

In this paper, a broadband THz linear frequency modulated continuous wave (LFMCW) imaging system is developed for the express purpose of NDT, especially for the detection of thick non-metallic materials. And two sets of FMCW experimental platforms are set up to assist the planning, preliminary investigation, and completion of this research project, including a narrow-band LFMCW 3D imaging radar

and a broader bandwidth THz stepped-frequency modulated continuous wave (SFMCW) 3D imaging radar. In Section II, these systems are described in detail, and their characteristics and key parameters are summed up. Section III introduces the imaging algorithms applicable to these systems that are efficacious in detecting different materials and various defects. In Section IV, the experimental results and analyses are given for actual objects with various materials and different defects, which convincingly demonstrate the ability of the developed systems to perform NDT. Section V provides a brief summary and a projection of follow-up work.

II. SYSTEM SETUP

For the THz CW systems, our exploration began with two-dimensional (2D) imaging radar [41], but due to its lack of characterization in the range direction, we continue to develop a broadband 3D imaging radar. Most of the THz radar imaging systems are mainly designed for long-range scenarios such as atmospheric remote sensing, missile guidance, and stand-off security inspection, whose requirements for accuracy of ranging and imaging are not as stringent as NDT. In this paper, 3D THz imaging radar with high range resolution is the main focus. With the exception of the SynView300 system, there is little previous research in this area. Moreover, for integration, portability, and engineering application, the system must be separated from the laboratory equipment. However, in order to be more reliable, two sets of experimental systems, including a narrow-band LFMCW 3D imaging radar and a wide-band SFMCW 3D imaging radar, are set up before studying the large bandwidth portable system, namely the wide-band LFMCW 3D imaging radar.

A. TWO SETS OF FMCW EXPERIMENTAL SYSYEMS

1) NARROW-BAND LFMCW 3D IMAGING RADAR

The frequency of the system determines the following selection of the sources, and it is also limited by some factors, such as currently available terahertz electronic devices and the application of NDT. Therefore, the approximate frequency of the broadband 3D imaging system is discussed in advance and it is determined to be around 200 GHz. This choice is based on three reasons. First, electromagnetic wave with frequency lower than 500 GHz, there are fewer water absorption peaks in the atmosphere and less transmission loss in medium [43]. Second, due to the limitation of THz solid-state electronic devices such as frequency multiplier and harmonic mixer, the higher the frequency is, the lower the conversion efficiency and transmission power are. The transmission power of 200 GHz is suitable for NDT. Third, compared with the lower frequency such as 100 GHz, a wider bandwidth and a larger ratio of bandwidth to center frequency can be achieved near 200 GHz. Therefore, the center frequencies of the two experimental systems are both around 200 GHz.

As a preliminary attempt to develop a 3D system independently, we built a band LFMCW 3D imaging radar

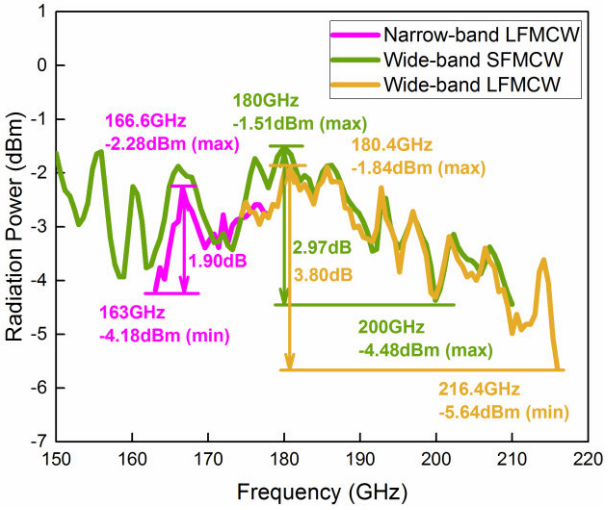

FIGURE 1. Full-band power spectrum.

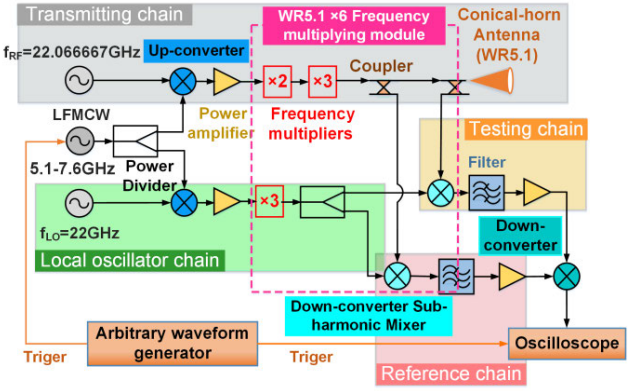

FIGURE 2. Block diagram of narrow-band LFMCW 3D imaging radar.

whose bandwidth is only 15 GHz (163-178 GHz). Due to its narrow bandwidth, the power flatness is excellent, with a maximum deviation of 1.9 dB, as shown by the pink curve in Fig. 1. Its block diagram is shown in Fig. 2. The signal of 22 GHz is supplied by a dielectric resonator oscillator from SAGE millimeter Inc, whereas that of the 22.0667 GHz is provided by a Vector Signal Generator E8267D from Agilent Technologies. Moreover, an analog slope sweep signal of 5.1 GHz to 7.6 GHz is generated through an RF signal generator from China Electronics Technology Instruments, whose sweep time is at least 25 ms. An arbitrary waveform generator and an oscilloscope are used for triggering and acquisition, respectively. The rest of the circuit is made up of passive elements. Compared with lower-frequency bands, terahertz electronic devices are more expensive, so it is hoped that they can continue to be re-used in subsequent high-bandwidth radar systems without wasting resources thus saving costs. The frequency multiplier is the core of the link to realize terahertz wave, and many adjutant devices are needed to go with it, such as power amplifier, coupler, subharmonic mixer. The link will also be mentioned many times in the

following. To avoid repetition, it is summarized as a WR5.1 ×6 frequency multiplying module, as shown inside the dotted box in Fig. 2.

In a broadband radar, the synchronization and phase coherence between the transmitting and local oscillator links should be guaranteed for accurate ranging and 3D imaging. To that end, a coherent super heterodyne detection scheme is often adopted. But in a common coherent structure, only the phase coherence of the signal source is considered, and the time delay caused by the imbalance of the transmission and local oscillator (LO) chains and the characteristics of other devices is ignored. For this reason, a full coherent super heterodyne structure is proposed in terahertz band, in which the reference signal is directly obtained from the down conversion of the transmission signal and the LO signal in terahertz band, and the influence of other elements are all taken into account. In addition, with the rapid development of THz electronic devices, their performance is constantly improving and their cost is gradually reduced, which provides the possibility for the realization of a full coherent structure.

Radar is often used in large scenes with transmission distance of several meters or even thousands of meters, such as in atmospheric remote sensing, missile guidance, vehicle distance measurement and security inspection [44], [45]. So the space between two antennas is almost negligible relative to the detection distance, and the system is regarded as quasi-monostatic. The transmitting and receiving antennas are often separated in parallel or the transmission path of one of them is changed by adding a spectroscope. The biggest advantage is to reduce the direct coupling of the transceiver, and to improve the SNR and dynamic range. Whereas in NDT, the testing distance is only a few millimeters or centimeters, and the distance between two antennas cannot be ignored. Then according to the reflection theorem, the transmitting and receiving antennas should be placed at an appropriate angle, which will require a complex system design that is not generally conducive to engineering, and the resulting system has to be operated by professionals. It is necessary to determine the optimal distance and angle between the two antennas according to their parameters and experimental requirements. Moreover, if the radial distance changes, the optimal distance and angle will also be adjusted accordingly. Although a beam splitter can avoid the above problems, the other elements must also be precisely arranged and controlled, which is detrimental to integration and portability. Under the condition of maintaining both the SNR and dynamic range, a coupler is used to realize the isolation of the transceiver, so that a single antenna design is adopted, which can not only improve the ranging accuracy, but also simplify the system structure.

The time-frequency diagram of LFM source is shown in Fig. 3. Since Δt is tiny (nanosecond level), the emission and acquisition are triggered synchronously, as shown in Fig. 2. And the acquisition time is slightly longer than the emission, so only start-stop scanning is applicable here. From Fig. 3, the ranging principle of FMCW can be analyzed.

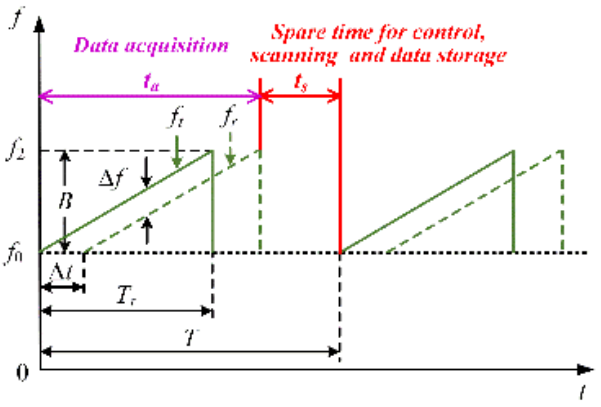

FIGURE 3. Time-frequency relation. f_0 is the start frequency, f_2 is the stop frequency; f_t and f_r represent the frequencies of the transmitted and reflected signals, respectively. T is the frequency sweep period.

In Fig. 2, there is a harmonic difference that multiplications of ×3 and ×6 are respectively applied for the LO and transmitted chains. Even though this does not impact the result due to the sub-harmonic mixing, it needs to be properly clarified that the LO signal in the following equation is defined as the result after sub-harmonic mixing. The transmitted signal and LO signal are respectively:

$$S_t(t) = A_t \cos\left[\left(f_0 + \frac{k}{2}t\right)t + \varphi_t\right], \tag{1}$$

$$S_{LO}(t) = A_{LO} \cos\left[\left(f_0 - f_d + \frac{k}{2}t\right)t + \varphi_{LO}\right], \tag{2}$$

where, f_0 is the start frequency, and A_t and φ_t are the amplitude and initial phase of the transmitted signal respectively; $k = B/T_r$ is the slope of the frequency modulation (FM), where B is the bandwidth, and T_r is the FM time. Here A_{LO} and φ_{LO} are the amplitude and initial phase of the LO signal, respectively. And f_d is the frequency difference between the transmitted signal and the LO signal.

The echo signal is

$$S_r(t) = \eta A_t \cos\left\{\left[f_0 + \frac{k}{2}(t - \Delta t)\right](t - \Delta t) + \varphi_t\right\}, \tag{3}$$

where η is the amplitude reflection coefficient of the echo signal, and Δt is the time delay between the echo signal and the transmitted signal.

The transmitted signal and the echo signal are respectively mixed with the LO signal to obtain the reference signal $S_{ref}(t)$ and the test signal $S_{mea}(t)$, and the intermediate frequency (IF) signal $S_{IF}(t)$ is obtained from the second mixing:

$$S_{ref}(t) = \frac{A_t A_{LO}}{2} \cos(f_d t + \varphi_t - \varphi_{LO}), \tag{4}$$

$$S_{mea}(t) = \frac{\eta A_t A_{LO}}{2} \cos\left[(f_d - k\Delta t)t - f_0 \Delta t + \frac{k}{2}\Delta t^2 + \varphi_t - \varphi_{LO}\right], \tag{5}$$

$$S_{IF}(t) = \frac{\eta A_t^2 A_{LO}^2}{8} \cos\left(-kt\Delta t - f_0\Delta t + \frac{k}{2}\Delta t^2\right), \quad (6)$$

The relation between frequency Δf and time delay Δt of the IF signal is

$$\Delta f = k\Delta t = \frac{B}{T_r}\Delta t, \quad (7)$$

The relation between the time delay Δt and the distance R is:

$$\Delta t = \frac{2R}{v}, \quad (8)$$

where v is the propagation speed of THz wave in medium. The range is available as

$$R = \frac{vT_r}{2B}\Delta f, \quad (9)$$

From (9), the key to get the distance is to get the frequency of IF signal by Fast Fourier Transform (FFT). Take the derivative of both sides of (9), and use the relation $\Delta(\Delta f) = 1/T_r$, the range resolution is obtained as

$$\Delta R = \frac{vT_r}{2B}\Delta(\Delta f) = \frac{v}{2B}, \quad (10)$$

For this system, the range resolution is 10 mm in free space.

2) WIDE-BAND SFMCW 3D IMAGING RADAR

The realization of super bandwidth near 200 GHz is discussed in terms of a wide-band SFMCW 3D imaging radar, which has been introduced before [8]. It is mainly composed of vector network analyzer (VNA) and WR5.1 ×6 frequency multiplying module. Fig. 4 shows the overall block diagram including broadband radar, scanning platform with controller and computer, and elaborates the connection and coordination between the units.

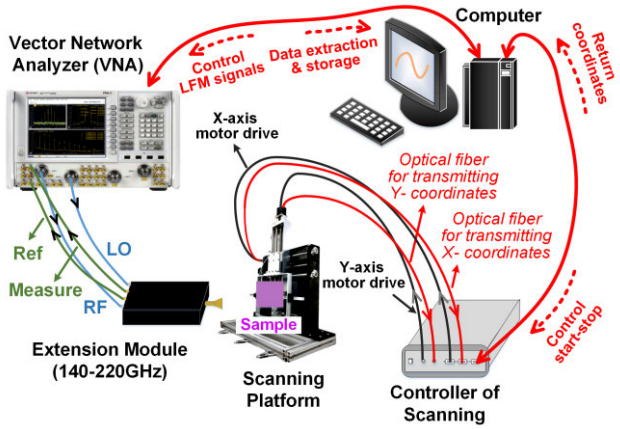

FIGURE 4. Overall block diagram of wide-band SFMCW 3D imaging system.

The VNA (Agilent Model 5247) radiates SFMCW of 10 MHz to 67 GHz. It can provide RF and LO input signals for the WR5.1 ×6 frequency multiplying module at the same time with four channels. The VNA also contains IQ demodulation circuit and processing algorithm of S parameter, standing wave ratio (SWR), group time delay and so on. S11 is extracted as the echo data to reconstruct the target, which represents the reflection information. The frequency range of the WR5.1 ×6 frequency multiplying module is from 140 GHz to 220 GHz. Combined with power flatness, the maximum power difference between 150 GHz and 210 GHz is less than 3dB, as shown by the light green line in Fig. 1, which is a major factor to make this band our choice.

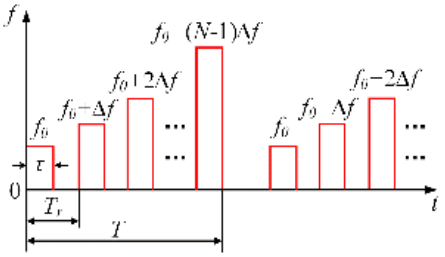

FIGURE 5. Time-frequency diagram of SFM in VNA. f_0 is the start frequency, Δf is the step frequency, and N is the total number of steps. τ and T_r are the duration and the period of each frequency, respectively. T is the frequency sweep period.

The time-frequency relation of the broadband THz signal emitted is shown in Fig. 5. Where the time τ is much smaller than T_r. In this wide-band SFMCW 3D imaging system, when N equals 1601 points, the period T is close to two seconds.

The transmitted signal is expressed as

$$S_t(t) = \sum_{i=0}^{N-1} A_i rect\left(\frac{t - iT_r - \frac{\tau}{2}}{\tau}\right) \cos\left[2\pi\left(f_0 + i\Delta f\right)t + \varphi_i\right], \quad (11)$$

where A_i and φ_i are the amplitude and initial phase of the $i+1^{\text{th}}$ pulse respectively, and $i = 0, 1, 2, \ldots, N-1$. And the echo signal is

$$S_r(t) = \sum_{i=0}^{N-1} A_i \eta_i(x, y)\, rect\left(\frac{t - iT_r - \frac{\tau}{2}}{\tau}\right) \cdot \cos\left[2\pi\left(f_0 + i\Delta f\right)(t - \Delta t) + \varphi_i\right], \quad (12)$$

where η_i represents the amplitude reflection coefficient of the $i+1^{\text{th}}$ pulse in the echo signal, Δt is the delay time of the echo signal relative to the transmitted signal. The LO signal is provided with a frequency difference f_d:

$$S_{LO}(t) = \sum_{i=0}^{N-1} A_i' rect\left(\frac{t - iT_r - \frac{\tau}{2}}{\tau}\right) \cdot \cos\left[2\pi\left(f_0 - f_d + i\Delta f\right)t + \varphi_i'\right], \quad (13)$$

where A_i' and φ_i' are the amplitude and initial phase of the $i+1^{\text{th}}$ pulse of the LO signal, respectively. Similar to LFMCW, test signal, reference signal and IF signal are

obtained, respectively as

$$S_{ref}(t) = \sum_{i=0}^{N-1} \frac{A_i' A_i}{2} rect\left(\frac{t - iT_r - \frac{\tau}{2}}{\tau}\right) \times \cos\left(2\pi f_d t + \varphi_i - \varphi_i'\right), \quad (14)$$

$$S_{mea}(t) = \sum_{i=0}^{N-1} \frac{A_i' A_i \eta_i(x,y)}{2} rect\left(\frac{t - iT_r - \frac{\tau}{2} - \Delta t}{\tau}\right) \cdot \cos\left[2\pi f_d t - 2\pi (f_0 + i\Delta f)\Delta t + \varphi_i - \varphi_i'\right], \quad (15)$$

$$S_{IF}(t) = \sum_{i=0}^{N-1} \frac{(A_i')^2 A_i^2 \eta_i(x,y)}{8} rect\left(\frac{t - iT_r - \frac{\tau}{2} - \Delta t}{\tau}\right) \cdot \cos\left[-2\pi (f_0 + i\Delta f)\Delta t\right], \quad (16)$$

In order to simplify (16), let $A_{IF} = \frac{(A_i')^2 A_i^2 \eta_i(x,y)}{8}$, and an analytic form is selected. Thus,

$$S_{IF}(t) = \sum_{i=0}^{N-1} A_{IF} rect\left(\frac{t - iT_r - \frac{\tau}{2} - \Delta t}{\tau}\right) \cdot \exp\left[-j2\pi (f_0 + i\Delta f)\Delta t\right], \quad (17)$$

When $t = iT_r + \frac{\tau}{2} + \Delta t$, the discrete expression is

$$S_{IF}(i) = A_{IF} \exp(-j2\pi f_0 \Delta t) \exp(-j2\pi i \Delta f \Delta t), \quad (18)$$

For a static target, the first exponential term is a fixed term, and the second exponential term can be regarded as a discrete frequency domain signal at a certain time. Therefore, time delay Δt can be calculated by inverse Fast Fourier Transform (IFFT) of (18). Let $k_0 = [N\Delta f \Delta t]$, and $[\cdot]$ means taking the integer. IFFT leads to

$$s_{IF}(k) = \left|\frac{1}{N} A_{IF} \frac{\sin \pi (k - k_0)}{\sin \frac{\pi}{N}(k - k_0)}\right| \cdot \exp(-j2\pi f_0 \Delta t) \exp\left[-j\left(\frac{k - k_0}{N}\right)\frac{N-1}{2}\right], \quad (19)$$

The modulus of $s_{IF}(k)$ is

$$s_{IF}(k) = \left|\frac{1}{N} A_{IF} \frac{\sin \pi (k - k_0)}{\sin \frac{\pi}{N}(k - k_0)}\right|, \quad (20)$$

When $k = k_0 = [N\Delta f \Delta t]$, the delay time Δt can be obtained by finding the main peak in the amplitude-frequency graph. The distance is

$$R = v\Delta t = \frac{v k_p}{2N\Delta f}, \quad (21)$$

where v is the propagation speed of THz wave in the medium, and k_p is the position of the main peak.

Taking the derivative of both sides of (21), the range resolution is obtained as

$$\Delta R = \frac{v}{2N\Delta f}, \quad (22)$$

For this SFMCW system, the range resolution is 2.5 mm in free space. From (10) and (22) it can be seen that for LFMCW and SFMCW, the range resolution is related to the material properties and the system bandwidth only.

B. WIDE-BAND LFMCW 3D IMAGING RADAR

Unlike the two sets of 3D imaging radars mentioned above, the broadband LFMCW system is our ultimate goal and has been described in detail in [46]. It is based on all solid state electronic technology, wideband linear frequency modulation ranging principle, full phase-coherent super-heterodyne detection structure and phase-locked frequency synthesis technology. Information on the time-frequency relation of this system has been introduced in [46]. At the same time, we propose a calibration process before testing the target, which can effectively improve the frequency linearity and ranging accuracy of the system [46]. The block diagram and photograph of the system are shown in Fig. 6. The frequency range is 174-216 GHz, and the ratio of bandwidth to central frequency is as high as 21.5%. The power flatness of the full band is slightly greater than 3dB, as shown by the yellow line in Fig. 1. By an ultra-broadband LFM source with Oven Controlled Crystal Oscillator, phase locked loop and Voltage-Controlled Oscillator, the digital LFM is realized with better sweep linearity, and the frequency sweep time can be as short as 2.8 ms.

The main parameters of the imaging systems above are summarized in Table 1. Compared with wide-band LFMCW 3D imaging radar, the narrow-band LFMCW radar in sub-subsection II-A-1) has lower center frequency, narrower bandwidth, poor spatial resolution, and an analog frequency sweep mode with poor linearity; the wide-band SFMCW radar has longer frequency sweep time and depends on larger external instrument (VNA), so it is not amenable to portability and unsuitable for engineering applications.

III. SIGNAL PROCESSING AND SIMULATION

The radar imaging hardware acts as a detector. It must be combined with signal processing to realize 3D imaging. This section is devoted to discussion of imaging related signal processing in conjunction with the hardware platforms discussed heretofore.

For NDT based on THz FMCW radar, different imaging algorithms can be adopted according to the different materials or defect positions of the target to be tested, so that the image will be clearer and the detection results can be more accurate. In this section, common NDT scenarios are discussed, which are divided into four categories. And the corresponding algorithms are introduced.

A. RANGING

Compared with single-frequency radar, the processing algorithms are much more complex for broadband FMCW radar. The biggest difference is the resolution capability in the range direction, as one-dimensional ranging is an important application for FMCW radar. In subsection II-A, FFT or IFFT is applied to get the range information. Although FFT has high calculation efficiency, there are some problems such as window truncation, energy leakage and fence effect, which make the frequency deviate from the IF signal, resulting

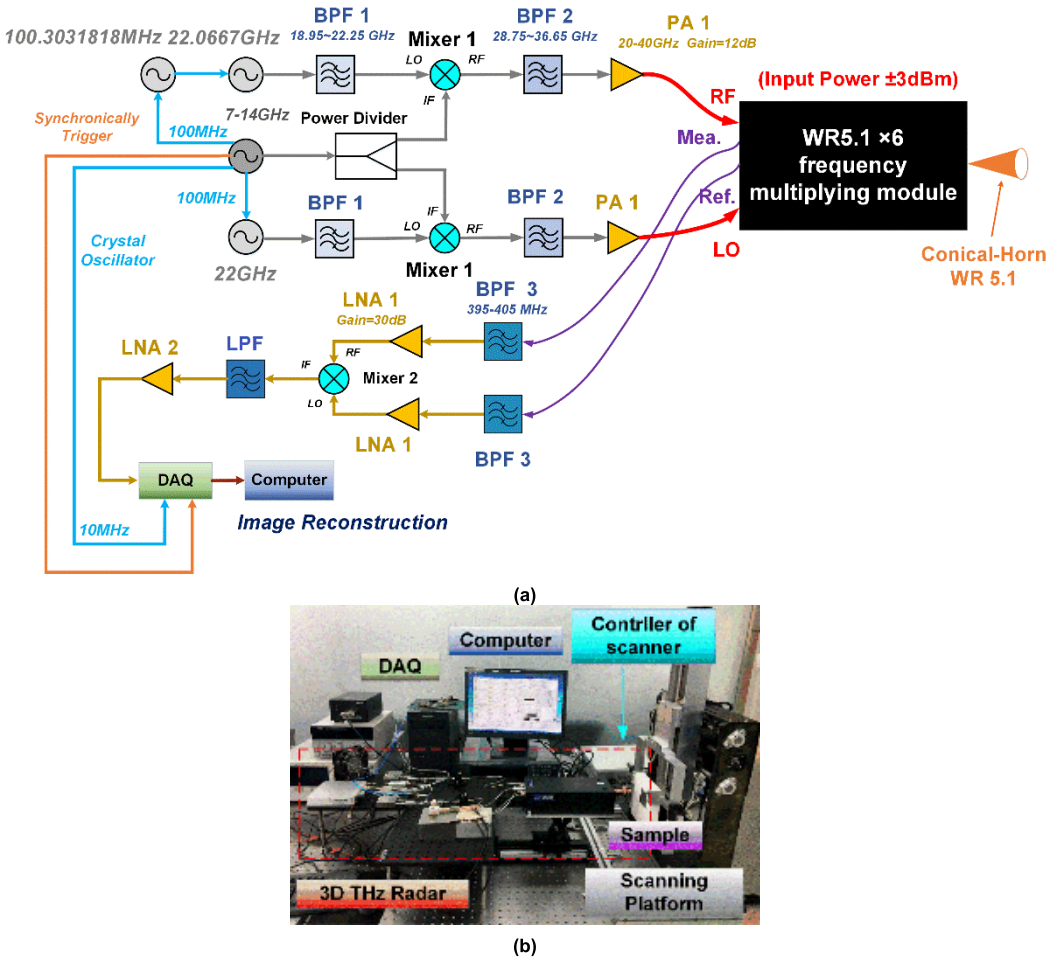

FIGURE 6. Wide-band 3D imaging radar system: (a) Block diagram, (b) Photograph of the system.

in inaccurate ranging. In long-distance detection, system performance is not sensitive to the above deviation. But in NDT, the detection distance is shorter and the target is thinner, so the above deviation will have a greater negative impact and further data processing is needed to improve the accuracy.

The fundamental reason for the problems of FFT is that the length of data collected is limited, which is equivalent to windowing. So the window function is the key to the following discussion. As shown in Fig. 7, the black curve is the real spectrum of the time-domain window function, but the discrete blue spectrum is obtained through FFT. Zero-padding is usually used to improve the accuracy, whereas it probably increases the data size and lead to larger computational burden and longer processing time. Therefore, spectral correction is introduced to obtain a more accurate spectrum without increasing the data length. Discrete spectral correction methods are mainly divided into amplitude-spectrum-based interpolation, phase difference correction, and energy centrobaric method [47]–[49]. Amplitude-spectrum-based interpolation is commonly used, which mainly corrects the main peak using two or three spectral lines with the largest amplitude. And in noisy

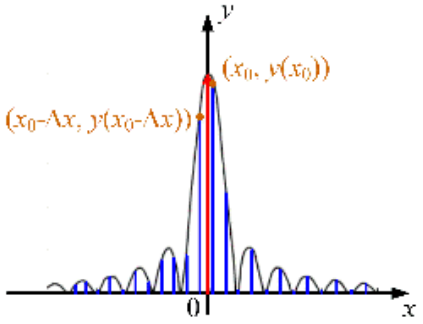

FIGURE 7. Comparison between the discrete spectrum obtained by FFT (blue line) and the real one (black line).

surroundings, the two-line amplitude-spectrum-based interpolation is more suitable and results in faster computation.

Regardless of the type of window function employed, its FFT spectrum is generalized as $y = f(x)$ as shown in the discrete blue spectrum of Fig. 7. The FFT number is N and the frequency interval is Δx. According to the window spectrum after FFT, the amplitude ratio of two adjacent spectral lines

TABLE 1. Characteristics and key parameters of systems.

Parameters	Narrow-band LFMCW 3D imaging radar	Wide-band SFMCW 3D imaging radar	Wide-band LFMCW 3D imaging radar
Center Frequency	170.5GHz	180GHz	195GHz
Bandwidth	15GHz	60GHz	42GHz
FM Waveform	LFMCW	SFMCW	LFMCW
Operating mode	Active Reflective	Active Reflective	Active Reflective
Radiation power	0.5mW	0.5mW	0.5mW
Power flatness	1.9dB	2.97dB	3.799dB
Frequency step	Analog scanning	37.5MHz	50KHz
Shortest frequency sweep time/period	10ms/100ms	1.6s/1.6s	2.8ms/2.8ms
Horn aperture	8.4mm	8.4mm	8.4mm
Horn full 3dB beamwidth	13 deg	13 deg	13 deg
Waveguide band	WR5.1	WR5.1	WR5.1
Beam spot size (10mm away)	3.12mm	2.92mm	2.4mm
Cross-range resolution (10mm away)	1.56mm	1.46mm	1.2mm
Range resolution (in free space)	10mm	2.5mm	3.2mm
Synchronous clock	No	Yes	Yes
Raster scanning manner	Start-Stop-Start	Start-Stop-Start	Start-Stop-Start
Scanning speed	3.3s/pixel	7s/pixel	1.9s/pixel
Application Scenario	Only Laboratory	Only Laboratory	Laboratory & field testing

at x and $(x - \Delta x)$ is constructed:

$$a(x) = \frac{f(x)}{f(x - \Delta x)}, \tag{23}$$

The inverse function of (23) is

$$x = g(a) \tag{24}$$

The highest and second-highest lines are located on either side of the main peak of the actual spectrum (the black curve in Fig. 7), and they are denoted as $(x_0 - \Delta x, f(x_0 - \Delta x))$ and $(x_0, f(x_0))$. Moreover, the spectrum of commonly employed windows are known, such as rectangular window and Hanning window, and the frequency offset caused by FFT can be calculated by using (23) and (24). Then the amplitude calculated by FFT can be revised to the actual one according to the obtained frequency offset. If the peak of the spectrum after FFT is at term M and the Hanning window is chosen, the correction results of frequency and amplitude are as follows:

$$f = (M + \Delta N)\,\Delta f, \tag{25}$$

$$A = 2\left(1 - \Delta N^2\right)\frac{\pi \Delta N y_M}{\sin(\pi \Delta N)}, \tag{26}$$

where

$$\Delta N = \begin{cases} \dfrac{2y_{M+1} - y_M}{y_{M+1} + y_M}, & y_{M+1} \geq y_{M-1} \\ \dfrac{y_M - 2y_{M-1}}{y_M + y_{M-1}}, & y_{M+1} \leq y_{M-1}, \end{cases} \tag{27}$$

The validity of the spectral correction is verified by simulation. The simulation parameters are the same as those of the wide-band LFMCW 3D imaging radar with bandwidth of 42 GHz, FM time of 56 ms, and sampling rate of 50 kHz. Two targets are respectively located at the distance of $d_1 = 50$ mm and $d_2 = 70$ mm. Then the IF signal can be expressed as:

$$x_{IF}(t) = \cos(2\pi f_{IF1} t) + \cos(2\pi f_{IF2} t), \tag{28}$$

According to (9), f_{IF1} and f_{IF2} are the frequencies corresponding to the two targets respectively, which are considered as "thin" objects or interfaces in comparison with the range resolution. The propagation speed of THz wave in free space is used here, which is equal to 3×10^8m/s. The frequency and amplitude through FFT and after the spectral correction by (25)-(27) are shown in Table 2, which demonstrates that the latter is obviously closer to the theoretical value.

If there is frequency interference and multiple frequency components are mixed with the main peak, the above spectral correction approach is not applicable. As an example, we consider the case where the simulation environment is the same as the previous one, but two targets are located at the distance of $d_1 = 500$ mm and $d_2 = 505$ mm, respectively. The spectrum by FFT only has one main peak. In order to apply spectral correction, the two frequency components are divided into independent main lobes by spectral refinement [50], here with the Chirp Z-Transform (CZT) [51]. The frequency and amplitude by CZT and after spectral correction are shown in Table 2. The latter is seen to be closer to the theoretical value.

However, when the frequency components differ by a frequency that is less than the waveform resolution, it is difficult to solve the frequency interference problem by spectral refinement. Super-resolution modern power spectral estimation schemes have been proposed to deal with

TABLE 2. Frequency and amplitude of IF signal by spectrum correction.

Targets' location	Frequency and amplitude of IF signal		
	Theoretical value	FFT/CZT	Spectrum correction/MUSIC/ESPRIT
50 mm	250 Hz, 1	250.1 Hz, 0.98 (FFT)	250.1 Hz, 1.00 (Spectrum correction)
70 mm	350 Hz, 1	357.3 Hz, 0.77 (FFT)	350.1 Hz, 1.00 (Spectrum correction)
500 mm	2500 Hz, 1	2500Hz, 0.9564 (CZT)	2500 Hz, 1.1258 (Spectrum correction)
505 mm	2525 Hz, 1	2527Hz, 0.9564 (CZT)	2526 Hz, 1.1261 (Spectrum correction)
500 mm	2500 Hz, 1	2506 Hz, 1.211 (CZT)	2500Hz, 2509Hz (MUSIC)
502 mm	2510 Hz, 1		2501Hz, 2511Hz (ESPRIT)

problems like this, such as multiple signal classification (MUSIC) [52] and estimation of signal parameters via rotational invariance techniques (ESPRIT) [53]. We illustrate this by the example where the simulation environment is the same as the first two simulations, but the two targets are located at the distance of $d_1 = 500$ mm and $d_2 = 502$ mm. The frequency results of IF signal by FFT, MUSIC and ESPRIT are shown in Table 2. This demonstrate that the modern power spectral estimation schemes can lead to more accurate frequency discrimination for extremely adjacent targets.

B. IMAGING OF SURFACE AND SUBSURFACE INTERNAL STRUCTURE OF MATERIALS WITH LOWER REFRACTIVE INDEX

Based on the free-space Green's function formulation [54], the SAR algorithm is a linear and adaptive imaging method, which improves the two-dimensional resolution and is suitable for detecting the object's surface or metal samples, including buried objects with lower refractive index than the host [55]. Frequency domain SAR algorithm is the first choice for image reconstruction, which can realize pulse compression quickly and effectively by FFT based on the assumptions of range curve offset, platform motion and point spread uniformity [56]. RMA relies on less approximation than Range-Doppler algorithm (RDA), and is more accurate and efficient, but interpolation error is inevitable, which will cause defocus in the range direction [57]. In practice, efficiency and accuracy present contradictory demands. There is a frequency-domain method of phase shift migration algorithm (PSMA), which can not only realize fast calculation, but also has high precision and no interpolation error [58]. RMA and PSMA have been applied in radar imaging [56], [59], [60]. So here we simply provide their calculation flow chart and omit the detailed formula derivation, as shown in Fig. 8.

The electromagnetic simulation for metal blade in free space is carried out based on the finite difference time domain (FDTD) method. The shape and size of the target are shown in Fig. 9 (a).

The simulation parameters are set in accordance with the wide-band LFMCW 3D imaging radar. The sampling interval along the x-axis and y-axis is 0.5 mm, and the distance from the radiation source to the target is 10 mm. The metallic blades in Fig.9 (a) are placed in the center of the scanning

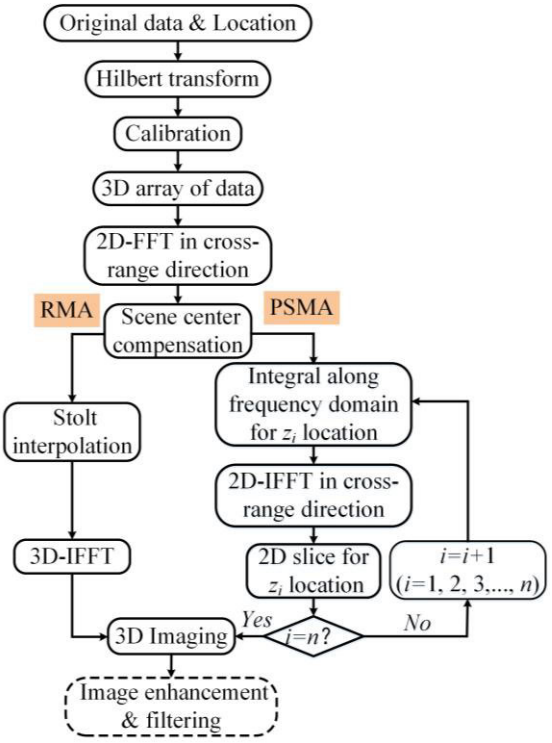

FIGURE 8. Flow chart of RMA and PSMA.

area. The reconstructed image by RMA and PSMA are shown in Fig. 9 (b) and (c). Their imaging results are similar, but compared with the result by PSMA in Fig. 9 (c), the focus position of metallic blades by RMA in Fig.9 (b) is deviated from the center of the scanned area. So the focus position of PSMA is more accurate.

C. IMAGING OF INTERNAL STRUCTURE OF MATERIALS WITH HIGHER REFRACTIVE INDEX

Although SAR algorithm has good focusing effect, it is no longer suitable for 3D image reconstruction of internal defects in materials with larger refractive index because of its reliance on the free-space Green's function. As shown in Fig. 10, the space is divided into air (region A) and sample (region B) containing defects (region C). Therefore, combining the half-space Green's function and exploding source model, a modified algorithm is proposed based on the SAR algorithm, which has been used in ground

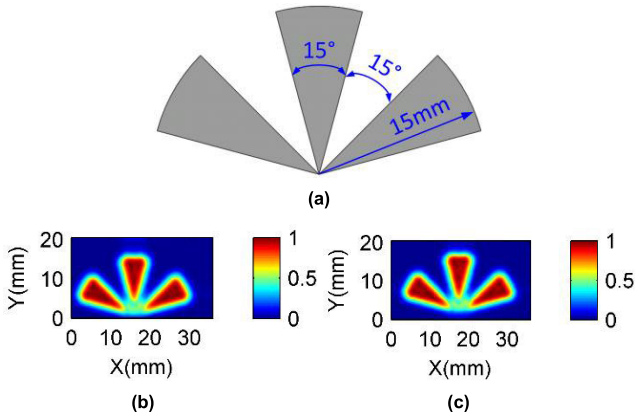

FIGURE 9. (a) Target in the form of metallic blades, (b) and (c)are the Imaging results of simulation: (b) RMA, (c) PSMA.

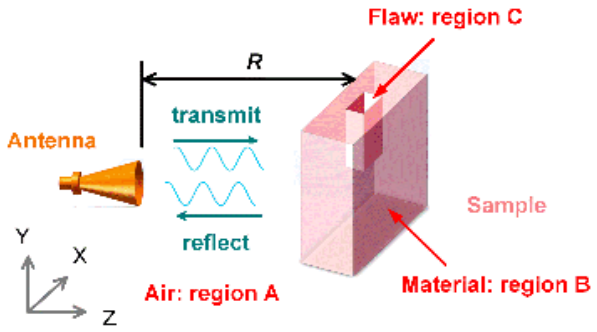

FIGURE 10. Position between antenna and target.

penetrating radar (GPR) previously [61]. In earlier research, the derivation procedure and simulation results of this algorithm have been carefully introduced in [8] and [46], and will not be detailed here.

D. IMAGING OF SLOPING OR CURVED SURFACES

In the above reconstruction algorithms, the surfaces of the targets are all flat. However, in many cases, it is necessary to detect the surface with a certain slope or curvature, and previous algorithms are no longer applicable. An algorithm combining frequency interference and phase unwrapping is proposed, which can improve the range resolution and realize surface detection of inclined and curved samples. According to (6), the delay time corresponding to the range is merely contained in the phase, so the amplitude is normalized. The IF signal is sampled with the time interval t_0, and the time axis is $t_1, t_2, \ldots, t_n$. The discrete IF signal is expressed as

$$S_{IF}(t_i) = \cos\left(-kt_i\Delta t - f_0\Delta t + \frac{k}{2}\Delta t^2\right), \quad i = 1, 2, \ldots, n, \tag{29}$$

where k is the slope of the frequency modulation. When $i = 1$,

$$S_{IF}(t_1) = \cos\left(-kt_1\Delta t - f_0\Delta t + \frac{k}{2}\Delta t^2\right), \tag{30}$$

The time-domain analytical signals of (29) and (30) are constructed by Hilbert transform [62]:

$$S_{IF}(t_i) = \exp\left[j\left(-kt_i\Delta t - f_0 t + \frac{k}{2}\Delta t^2\right)\right], \quad i = 1, 2, \ldots, n, \tag{31}$$

$$S_{IF}(t_1) = \exp\left[j\left(-kt_1\Delta t - f_0\Delta t + \frac{k}{2}\Delta t^2\right)\right], \tag{32}$$

The phase difference between the signal $S_{IF}(t_i)$ at t_i and t_1 can be obtained by the following equation, and the signal at t_1 plays the role of a reference.

$$\begin{aligned} &S_{IF}(t_i) \cdot conj\left[S_{IF}(t_1)\right] \\ &= \exp\left[j\left(-kt_i\Delta t - f_0\Delta t + \frac{k}{2}\Delta t^2\right)\right] \\ &\quad \cdot \exp\left[-j\left(-kt_1\Delta t - f_0\Delta t + \frac{k}{2}\Delta t^2\right)\right] \\ &= \exp\left\{j\left[k\left(t_i - t_1\right)\Delta t\right]\right\} = \exp\left\{j\left[k\left(i-1\right)t_0\Delta t\right]\right\}, \end{aligned} \tag{33}$$

In order to realize ranging, the delay time Δt should be obtained by dividing the phase $k(i-1)t_0\Delta t$ by the parameter $k(i-1)t_0$. But the directly extracted phase is usually wrapped around to $[-\pi, \pi]$ or $[0, 2\pi]$, so the unwrapped phase needs to be obtained before the division. The final equation for extracting the delay time can be sorted out as follows:

$$\Delta t = \frac{unwrap\left\langle angle\left\{S_{IF}(t_i) \cdot conj\left[S_{IF}(t_1)\right]\right\}\right\rangle}{k(i-1)t_0}, \tag{34}$$

where, *angle* $(\cdot)$ represents the process of obtaining the phase, and *unwrap* $(\cdot)$ is the process of unwrapping the phase. Then the tested distance is $R = c\Delta t/2$.

Compared with the above-mentioned algorithms, the range resolution of this method will not be limited by FFT and the system bandwidth. It can achieve high ranging accuracy, thus alleviating the problem of severe disparity between cross-range resolution and range resolution in 3D imaging, especially for narrow bandwidth systems. However, this method also has some shortcomings. First, it is only applicable to the detection of surface topography. Second, it mainly depends on the phase with high sensitivity and weak anti-jamming capability, so the SNR needs to be further improved in practical application.

Based on the FDTD method, the electromagnetic simulation of targets with tilted and curved surfaces is carried out, and the imaging performance of the algorithm is verified. The simulation parameters are the same as those of the wide-band LFMCW 3D imaging radar. The two targets are perfect electrical conductors (PEC), and denoted as sample A and B. Their shape and size are shown in Fig. 11 (a) and (b). The position between the emission source and the targets is shown in Fig. 11 (c) and (d).

In the range direction, the above-mentioned algorithm relies on FFT. In Fig. 12, the 3D reconstruction results of this algorithm and FFT are compared. Here, for FFT, the original length of the data is applied without zero-padding and spectrum refinement. The RGB color is independent of

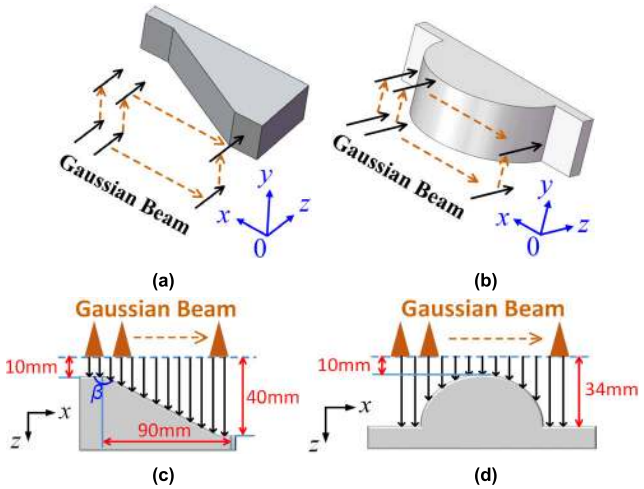

FIGURE 11. (a) and (b) show the shape and size of targets: (a) Sample A (an inclined planar surface), (b) Sample B (surface of circular arc). (c) and (d) show the spatial relation between the emission source and the targets: (c) Sample A, (d) Sample B.

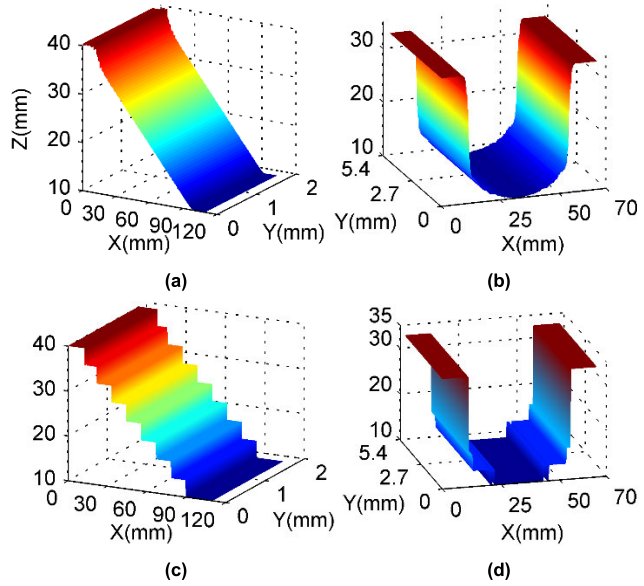

FIGURE 12. 3D imaging results of our algorithm and FFT. (a) Our algorithm for sample A, (b) our algorithm for sample B, (c) FFT for sample A, (d) FFT for sample B.

the amplitude reflection coefficient, and only represents the distance. The 3D imaging result of this algorithm is closer to the slope and curvature set in the simulation, whereas that of FFT is ladder-shaped, which deviates from the slope and curvature completely.

The slices are intercepted respectively at the middle of the Y-axis in Fig. 12 (a) and (b) to obtain the red line as shown in Fig. 13. In the enlarged circle in Fig. 13 (a), there is skew distortion. In Fig. 13 (b), the reconstruction results also deviate from the shape set in the simulation in the transition zone from arc to straight line. There are two main reasons for these deficiencies. First, in the transition zone, especially at the sharp angle, the electromagnetic scattering is complex. Second, for the convex arc (sample B) or the obtuse angle

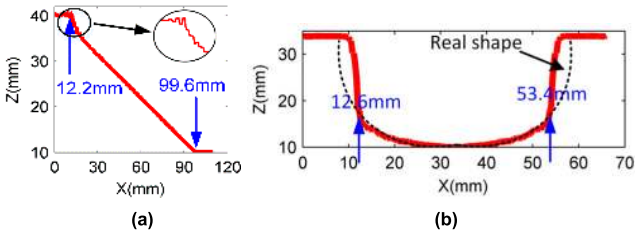

FIGURE 13. Slices are intercepted respectively at the middle of the Y-axis in Fig. 12 (a) and (b).

β (sample A), the electromagnetic wave will be scattered to other directions and cannot be received by the detector. Due to the limited machining precision, it is difficult to make sharp corners in the actual samples, instead, transition chamfers or fillets are usually used, so the first reason is not studied in depth. When the detector and the transmitter are located at different positions or angles, the problem caused by the second reason can be solved. However, in this paper, the single antenna transceiver is adopted. Then the detectable maximum convex radians are analyzed without changing the detection mode. And several sets of simulation experiments are added. The arc-shaped samples with radius of 50 mm, 70 mm and 90 mm are detected respectively, and the distance between the arc apex and the emission source is 10 mm. Similarly, in their 3D reconstruction images, 2D slices are intercepted along the middle position of the Y-axis to obtain the curves shown in Fig. 14 (a), (b) and (c).

By observing and comparing the reconstruction results of sample B and these three groups of samples, the measurable curvature range is obtained and the relationship between its size and the radius is analyzed. The calibration data of the angle γ in Fig. 14 (d) are listed in Table 3. It is found that the angle γ decreases slightly with the increase of radius, but the values are close to 58°.

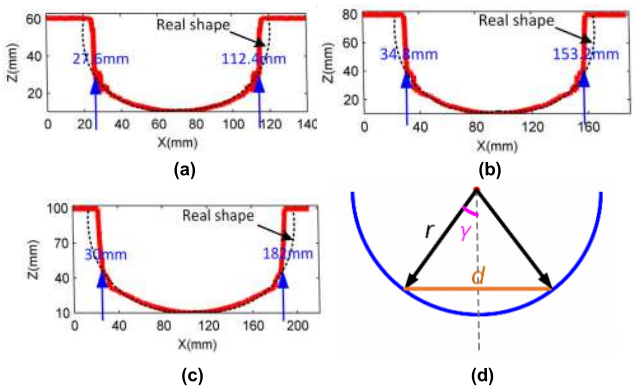

FIGURE 14. (a)-(c): 2D slices intercepted along the middle position of the Y-axis in 3D imaging results. Samples with the radius of (a) 50 mm, (b) 70 mm and (c) 90 mm. (d) The sketch of angle γ.

IV. IMAGING RESULTS AND ANALYSIS

A. SIMPLE 3D IMAGING OF TWO EXPERIMENTAL SYSTEMS

The two experimental systems are prepared for feasibility analysis of the LFMCW 3D imaging radar. Therefore,

TABLE 3. Comparison of angle Γ between different radii.

r (mm)	d (mm)	$\sin\gamma$	γ
24	40.8	0.850	58.2°
50	84.8	0.848	58.0°
70	118.	0.846	57.8°
90	152.0	0.844	57.6°

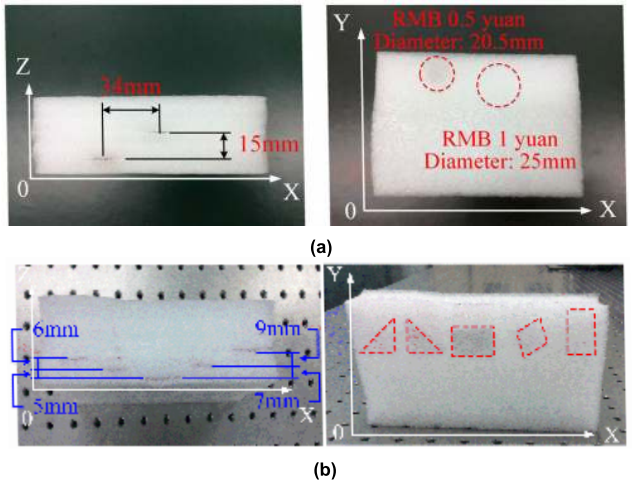

FIGURE 15. (a) Foam with embedded coins (0.5yuan and 1yuan), (b) Foam with different shape of metal sheets embedded.

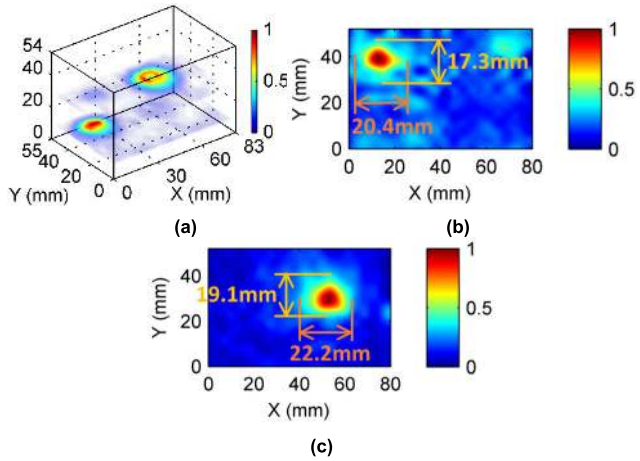

FIGURE 16. 3D imaging. (a) Slice stacking, (b) 2D slices at the range of 0.5 yuan coin, (c) 2D slices at the range of 1 yuan coin.

without electromagnetic reconstruction algorithm focusing, only simple signal processing is used such as applying FFT or IFFT to acquire the range information and no focusing on the cross-range directions for simple 3D imaging.

The narrow-band LFMCW 3D imaging radar is the first developed FMCW system with a certain bandwidth. The defect with high contrast to the background is taken as the target, such as the foam with coins or sheet metal inserted, as shown in Fig. 15. The 3D imaging results are displayed in Fig. 16 and 17.

For the wide-band SFMCW 3D imaging radar, a polytetrafluoroethylene (PTFE) board with a hole is selected as a sample, which represents the lower reflectivity contrast

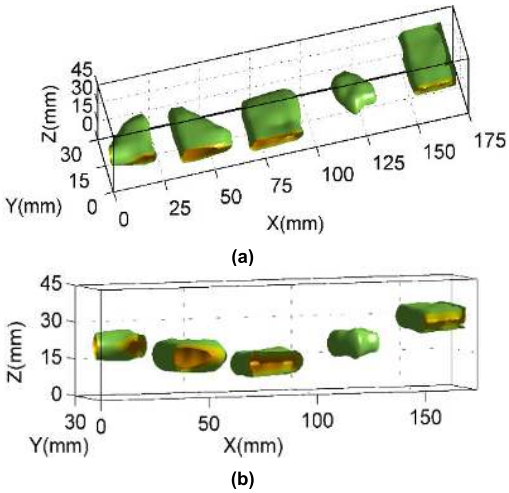

FIGURE 17. 3D isosurface imaging results of metal sheets of different shapes. (a) Face to YZ plane, (b) Look down to XY plane.

between the defect and the background material in the target. The shape of the target has been described in [8], and shown in Fig. 18. The 3D imaging result is obtained with IFFT in the range direction and without focusing on the cross-range directions, as shown in Fig. 18 (c)-(e).

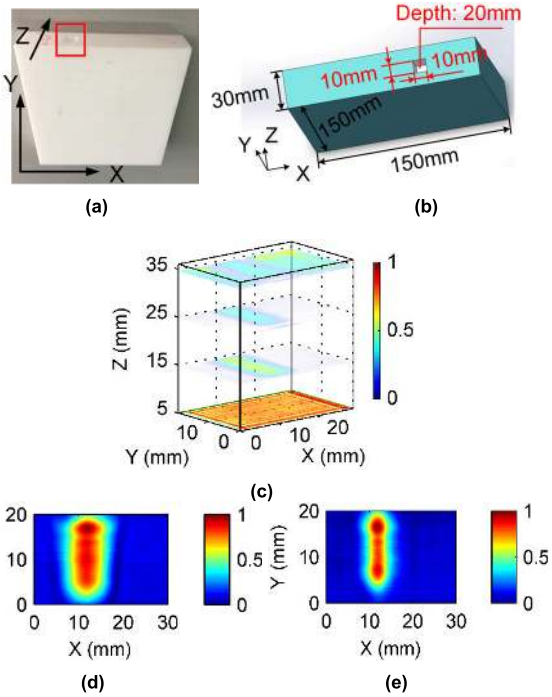

FIGURE 18. (a) and (b) show the photo and the 3D geometric model of Polytetrafluoroethylene (PTFE) board with a hole, respectively. (c), (d) and (e) show the 3D imaging results of the PTFE board, in which (d) and (e) are two-dimensional imaging slices at the distance between the front and rear surfaces of the hole respectively.

In Fig. 16 (b) and (c), the size of the coin is seriously distorted. In Fig. 17, the edges and corners of the triangular, square and rhombic metal sheets are blurred. In Fig. 18 (d) and (e), the shape of the hole is also distorted.

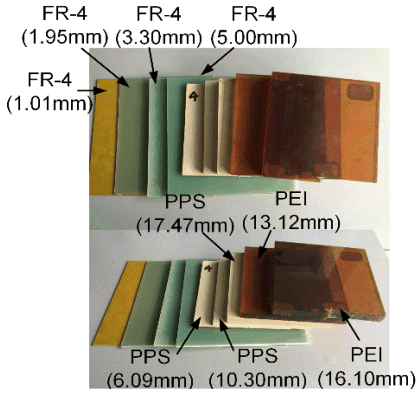

FIGURE 19. Photos of the plastic plates.

TABLE 4. Refractive indices of the plastic plates.

Material	Refractive index
Yellow FR-4 (yellow)	2.21
Green FR-4 (green)	2.15
Polyphenylene sulfide (PPS)	1.92
Polyetherimide (PEI)	1.75

These phenomena reveal the importance of the electromagnetic reconstruction algorithms in the subsection III-B and C.

B. WIDE-BAND LFMCW 3D IMAGING RADAR

1) RANGING

To test the ranging capability of the wide-band LFMCW 3D imaging radar, a number of plastic plates with different thickness are prepared. Their photos are shown in Fig. 19, with the thickness of each also marked, including all cases that are less than, close to, and greater than the range resolution. Their refractive index from 170 to 220 GHz are measured by a terahertz time-domain spectroscopy system (THz-TDS) without dispersion, and listed in Table 4. According to the refractive index and geometric thickness, the optical thickness can be calculated, as shown in Table 5.

In these experiments, the distance between the plastic plates and antenna is 100 mm, and the calibrator is 20 mm away from the antenna. So the range difference after calibration is 80 mm. Different methods introduced in subsection III-A, such as the spectrum correction, spectrum refinement, and modern power spectrum estimation, are used to process the calibrated time-domain analytical signal, and the thickness measurement results are shown in Fig. 20. The distance difference mainly reflects the inaccuracy from 80 mm because of the distance measurement error during manual placement and the slight positioning offset of each algorithm.

For the FR-4 plates with optical thicknesses of 2.21 mm and 4.30 mm, which are less than or close to the range resolution, MUSIC and ESPRIT are adopted. The thickness of 4.30 mm is slightly larger than the range resolution, and the "FFT + CZT + spectrum correction" can also be used. From Fig. 20 (a) and (b), FFT with zero compensation does not improve the thickness measurement accuracy, whereas the optical thicknesses obtained by MUSIC and ESPRIT are quite close to the actual value. For the FR-4 plate with the optical thickness of 4.30 mm, the "FFT + CZT + spectrum correction" is also effective.

For the FR-4 plates with optical thicknesses of 7.10 mm and 10.75 mm, and the PPS plate with an optical thickness of 11.70 mm, which are several times greater than the range resolution, "FFT + spectrum correction" are used and compared with "FFT + CZT + spectrum correction". From Fig. 20 (c), (d) and (e), it can be seen that "FFT + CZT + spectrum correction" is more accurate than "FFT + spectrum correction", and both are more accurate than FFT.

For the PPS plates with optical thicknesses of 20.28 mm and 33.54 mm, and the PEI plates with optical thicknesses of 22.93 mm and 28.18 mm, which are around 10 times larger than the range resolution, "FFT + spectrum correction" is suitable. From Fig. 20 (f), (g) and (h), the optical thickness

TABLE 5. Actual and tested optical thickness of plastic plates.

Material	Optical thickness (mm)	Tested optical thickness (mm)				
		FFT	MUSIC	ESPRIT	FFT+ spectrum correction	FFT+CZT+ spectrum correction
Yellow FR-4	2.21	-	2.2	2.4	-	-
Green FR-4	4.19	-	4.2	4.2	-	4.1
	7.10	7.5	-	-	7.0	7.1
	10.75	9.8	-	-	11.2	10.8
PPS	11.70	9.8	-	-	11.7	11.7
	19.78	19.6	-	-	19.7	-
	33.54	32.6	-	-	33.0	-
PEI	22.93	23.6	-	-	22.8	-
	28.18	26.1	-	-	28.1	-

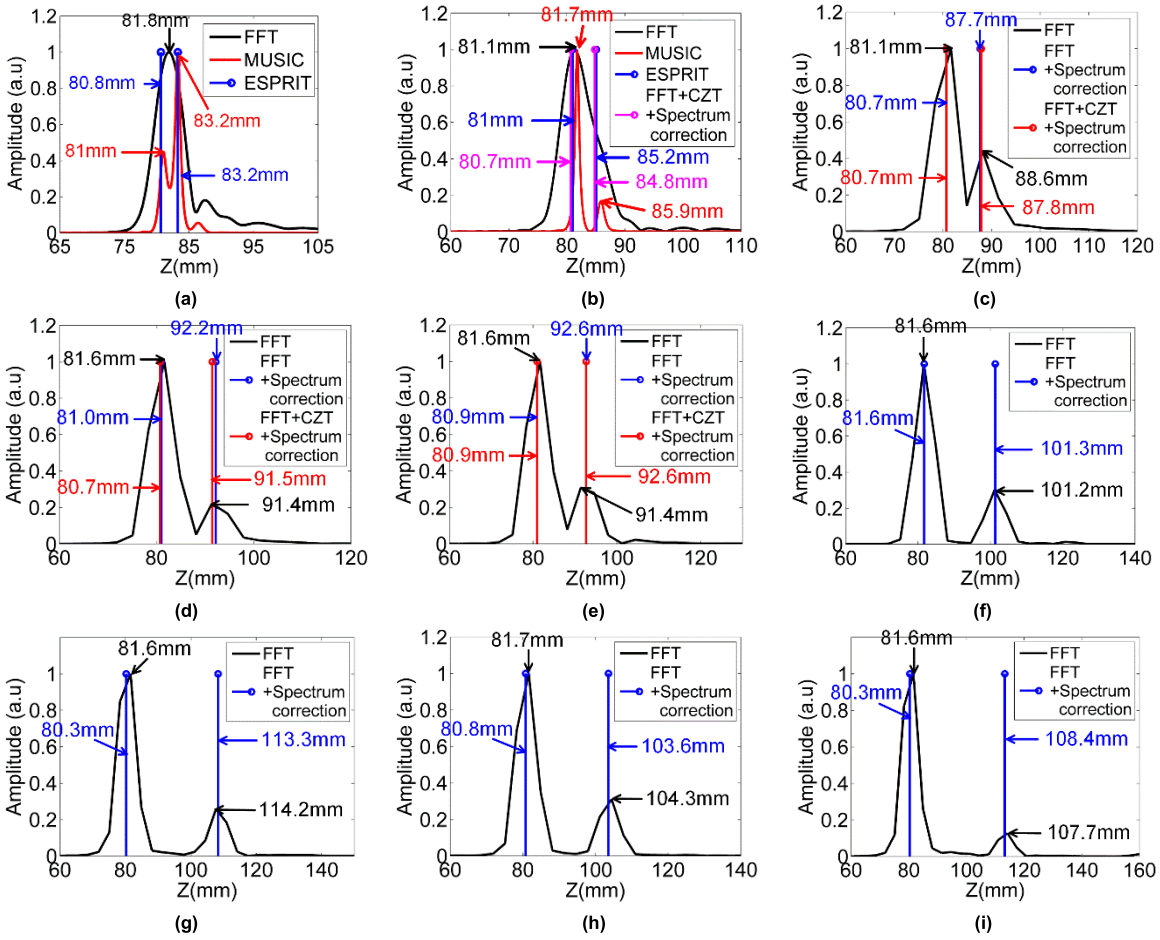

FIGURE 20. Optical thickness of plastic plates. (a) 2.21 mm FR-4, (b) 4.30 mm FR-4, (c) 7.10 mm FR-4, (d) 10.75 mm FR-4, (e) 11.70 mm PPS, (f) 20.28 mm PPS, (g) 33.54 mm PPS, (h) 22.93 mm PEI, (i) 28.18 mm PEI.

obtained by "FFT + spectrum correction" is more accurate and obviously better than FFT.

The tested optical thickness of all the plates are summarized in Table 5 and compared with the actual values, which better reflect the characteristics and advantages of each algorithm. It is generally believed that even for thicker samples, one more step of CZT can make the results more accurate, but by comparison between the samples with 10.75 mm and 11.70 mm thickness, it only has a good effect on the plate with thickness of 10.75 mm.

In conclusion, based on the above methods, the optical thicknesses of the samples can be accurately measured. On the other side, the unknown refractive indices can be calculated for the samples with known geometric thicknesses.

2) IMAGING OF INTERNAL STRUCTURE OF MATERIALS WITH LOWER REFRACTIVE INDEX

For surface imaging, the PCB board with metal strips on its top surface has been considered in [46], and the imaging results by RMA is excellent.

For the detection of internal structure of materials with lower refractive index, rigid PMI foam with multi-shaped metal sheets has been designed as a target, and their shapes and sizes are accurately imaged by RMA in [46]. However, the metal sheets are located at different positions of X, Y and Z in the foam. Another PMI foam with refractive index of 1.04 is prepared, which is inserted with multi-shaped polypropylene (PP) sheets located at different distances from the top surface, but the positions are overlapped in the XY plane, as shown in Fig. 21. In this case, an interesting question arises: if the terahertz wave passing through the front defect continues to transmit to the back defect, will the imaging of the back defect be covered by the shape of the front defect?

The 3D imaging results obtained by RMA and PSMA are shown in Fig. 22. The imaging results of the two SAR algorithms are similar. The testing distance is 10 mm and the scanning step is 0.5 mm. In Fig. 22 (a) and (b), from top to bottom are 2D slices parallel to the XY plane, intercepted at the distance of the triangular, rectangular and circular PP sheets. Compared with the imaging results of PMI foam with multi-shaped metal sheets in [46], the imaging performance of this experiment is not as good regardless of shape, size and consistency. There are three main reasons. First, the positions of the inclusion targets overlap with each other. When the

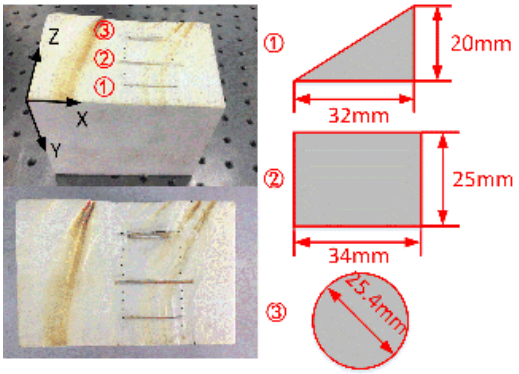

FIGURE 21. PMI foam with multi-shaped polypropylene (PP) sheets inserted in it, at the same X and Y location and different Z locations.

signal is transmitted to the back target, it has been reflected or scattered by the front target many times, and the system works in the reflection mode. In the return path, the signal will be reflected or scattered by the front target twice, so the triangular PP sheet can be seen faintly in the imaging results of the rectangular PP sheet. Second, the sample is handmade, in which a thin gap is first scraped with a thickness similar to that of the PP sheet with a knife and then the thin sheets are inserted. But in the deeper position of the foam, it is difficult for the knife to operate and the insertion mainly depends on hard external force. So, at the inner corners of each PP sheet, the foam becomes rough and chaotic due to extrusion, and the thin gap is made slightly wider. The scattering between the gaps also causes energy dissipation of the echo signal, thus affecting the imaging quality of the circular PP sheet. Third, in terms of reflectivity, the contrast between PP and foam is lower than that of metal and foam, which has a negative effect on imaging. Finally, in the PMI foam, the hole that is inserted by the circular sheet is wider and rougher than those with the rectangular and triangular sheets, which leads to the appearance of red spots in the images of the circle, making it difficult to discern the circle and this will also result in the slightly different positions of the circles. In addition, RMA and PSMA give slightly different positioning as well. Despite these problems, the location, shape and size of the insertions in the sample can be basically recognized from the imaging results in Fig. 22. If the sample is processed more precisely, the imaging results would be better.

To sum up, when the defect positions overlap, the front defects will affect the imaging performance of the back defects. However, the defect at its own range has the most impact and always dominates the signal, so the more obvious rectangular and circular shapes can be observed from the middle two images and the lower two images of Fig. 22, respectively.

3) IMAGING OF INTERNAL STRUCTURE OF MATERIALS WITH HIGHER REFRACTIVE INDEX

The refractive index of PTFE is 1.44 in the frequency band of 170 GHz to 220 GHz, which is also tested by THz-TDS.

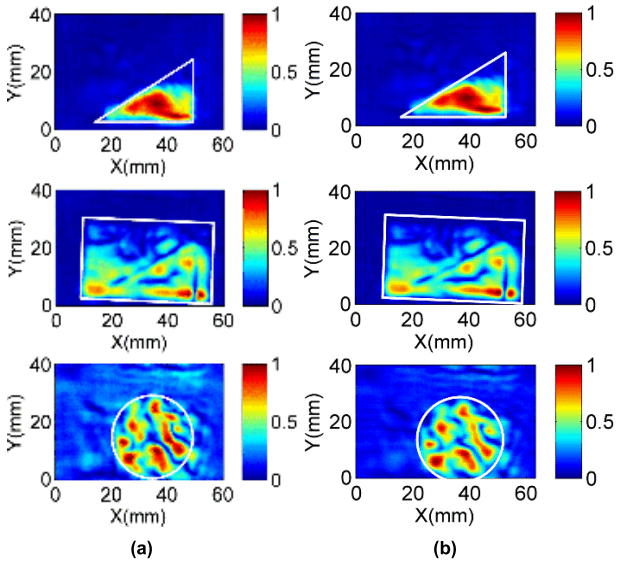

FIGURE 22. 2D slice imaging parallel to XY plane. (a) RMA,(b) PSMA.

The PTFE board with a hole represents the sample with higher refractive index, as shown in Fig. 18. It has been 3D-reconstructed by the modified algorithm based on the half space Green's function and exploding source mode in [46]. And its result has been compared with that of RMA, and shown to be superior. For example, the imaging results of defects obtained by this algorithm are closer to the rectangle (the real shape of the target), while the results obtained by RMA are more like ellipses [46].

4) IMAGING OF SLOPING OR CURVED SURFACES

Metallic samples with inclined and curved surfaces are prepared, as shown in Fig. 23.

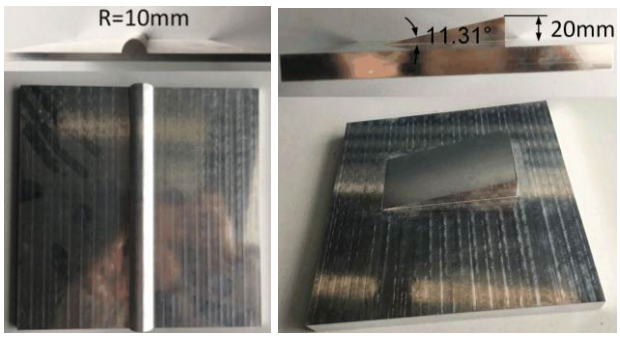

FIGURE 23. Metallic samples with curved or inclined surfaces: (a) cylindrical protrusion, (b) sloping planar protrusion ($\theta = 11.31°$).

The closest distance between the surface of the circular arc or the slope and the antenna is 10 mm, and the scanning steps are 0.2 mm and 0.3 mm respectively. Due to the sensitivity to slight phase variation and poor anti-interference ability, the tested data from the system is preprocessed by filtering and denoising, and then 3D imaging is realized

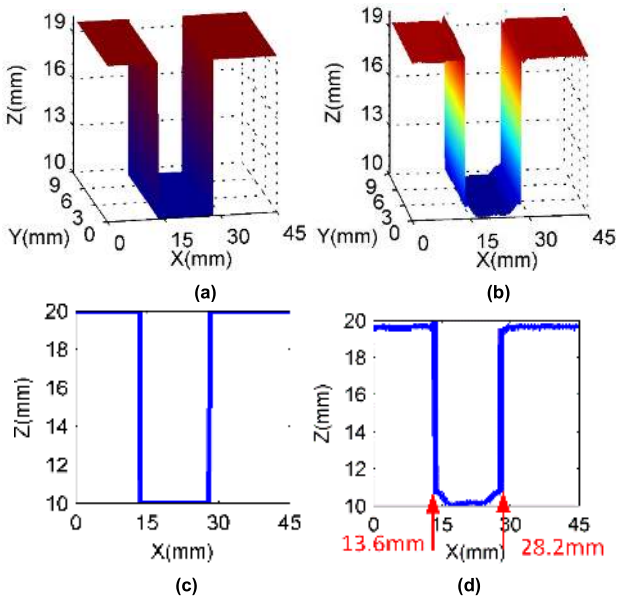

FIGURE 24. Imaging results of a metallic sample with curved surface: (a) 3D holography obtained by FFT, (b) 3D holography obtained by frequency interference algorithm, (c) curve intercepted in the middle of Y-axis of (a), (d) curve intercepted in the middle of Y-axis of (b).

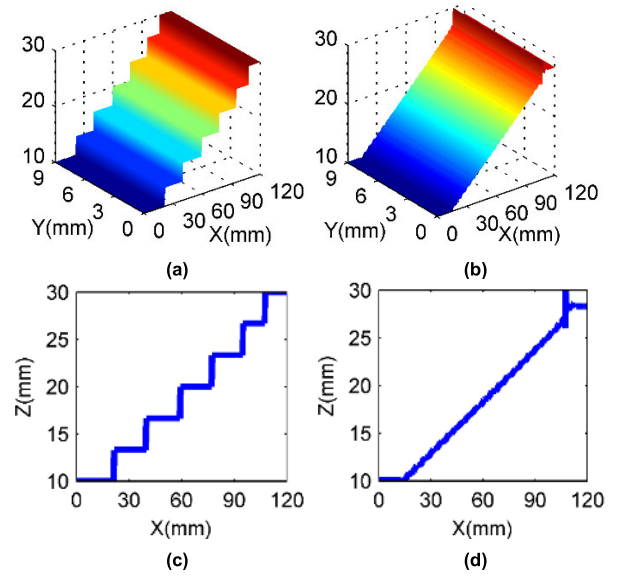

FIGURE 25. Imaging results of a metallic sample with sloping surface: (a) 3D holography obtained by FFT, (b) 3D holography obtained by frequency interference algorithm, (c) curve intercepted in the middle of Y-axis of (a), (d) curve intercepted in the middle of Y-axis of (b).

by FFT or a frequency interference algorithm. Here, for FFT, the original length of the data is applied without zero-padding and spectrum refinement. The results are shown in Figs. 24 and 25. Even with the additional preprocessing, the imaging performance of this experiment is still relatively poor compared with the simulation results in Fig. 12.

According to the imaging results in Fig. 24 (b) and (d), and referring to Fig. 14 (d), it is calculated that the angle γ that reflects the curvature testing ability is 46.9°, which is less than the 58° obtained by simulation. The size of angle γ is mainly affected by the edge scattering, and the radius of the cylindrical sample is small, so the arc range that can be successfully detected is limited. But compared with FFT, the imaging performance by frequency interference algorithm is better. From Fig. 25, for the sample with the inclined surface, the slope shape is more consistent with the real object by the frequency interference algorithm, whereas staircase-like by FFT. For the corner of the slope, the experimental imaging results obtained by the frequency interference algorithm are consistent with the simulation results in Fig. 13.

V. CONCLUSION

An active all-solid-state electronic terahertz broadband LFMCW imaging system has been developed for the specific purpose of NDT. Meanwhile, two sets of imaging platforms were used to assist the research, including a narrow-band LFMCW 3D imaging radar and a wide-band SFMCW 3D imaging platform. By comparison, the practicability and technical merits of the in-house-developed ultra-wideband LFMCW system is more prominent. For a 3D imaging system, it is necessary to consider the flatness, thickness, depth and material attributes of samples, so the reconstruction algorithm cannot be omni-purpose, but different reconstruction algorithms are proposed corresponding to the various application scenarios. The first is the accurate measurement of the object's thickness and distance. Spectral correction and refinement based on FFT and modern power spectral estimation are presented, which are applicable to wide ranges of distances and thicknesses. If the distance between the target and the antenna or target's thickness is much larger than the range resolution, "FFT + spectral correction" is suitable. If they equal to several times of the range resolution, the best can be selected from "FFT + spectral correction" and "FFT + spectral refinement + spectral correction" through a trial-and-error process. If they are slightly larger than the range resolution, "FFT + spectral refinement + spectral correction" and modern power spectral estimation are both available. And finally if they are very close to or even less than the range resolution, modern power spectral estimation schemes such as MUSIC and ESPRIT can achieve accurate result. The second is surface detection or internal detection of objects with low refractive index. Two frequency-domain synthetic aperture radar algorithms based on free-space Green's functions are employed to reconstruct 3D images of targets. The third is the interior detection of materials with large refractive index. A new modified algorithm based on half-space Green's functions and the explosion source model is proposed. The fourth is the measurement of the surface topography of inclined or curved objects. For such applications a new algorithm combining frequency interference with phase unwrapping is proposed and demonstrated, which overcomes the limitation of bandwidth and enables accurate detection of objects with inclination and curvature. Electromagnetic simulation of the above-mentioned scenarios are carried out based on FDTD, in which the parameters are set in accordance with the

corresponding systems, and the corresponding algorithms are applied to verify their effectiveness. For a variety of applications of NDT, data processing and reconstruction algorithms are discussed in detail, and algorithms from other fields are innovatively applied to terahertz imaging detection.

Finally, the systems and reconstruction algorithms are combined in action: a multitude of actual samples are irradiated and scanned by the systems to obtain the echo signals, and the appropriate reconstruction algorithm is selected to realize their 3D imaging. The hardware and algorithmic approaches developed and demonstrated in this project should be potentially valuable for applications in THz NDT of composite materials and structures.

REFERENCES

[1] C. Fan, M. Caleap, M. Pan, and B. W. Drinkwater, "A comparison between ultrasonic array beamforming and super resolution imaging algorithms for non-destructive evaluation," *Ultrasonics*, vol. 54, no. 7, pp. 1842–1850, Sep. 2014.

[2] C. Meola, S. Boccardi, G. M. Carlomagno, N. D. Boffa, F. Ricci, G. Simeoli, and P. Russo, "Impact damaging of composites through online monitoring and non-destructive evaluation with infrared thermography," *NDT E Int.*, vol. 85, pp. 34–42, Jan. 2017.

[3] M. Wang, F. Li, M. Zheng, W. Lu, Y. Jia, Q. Yu, S. Zhao, and J. Wu, "Realization of absolute-phase unwrapping and speckle suppression in laser digital holography," *Annalen der Physik*, vol. 529, no. 8, Aug. 2017, Art. no. 1600378.

[4] M. F. Kimmitt, "Restrahlen to T-rays—100 years of terahertz radiation," *J. Biol. Phys.*, vol. 29, nos. 2–3, pp. 77–85, Jun. 2003.

[5] M. Y. Liang, C. L. Zhang, R. Zhao, and Y. J. Zhao, "Experimental 0.22 THz stepped frequency radar system for ISAR imaging," *J. Infr., Millim., THz Waves*, vol. 35, no. 9, pp. 780–789, Sep. 2014.

[6] Y. Jiang, H. Wang, Y. Qin, B. Deng, J. Gao, and Z. Zhuang, "A three-dimensional surface imaging method using THz dual-frequency interferometry," *IEEE Geosci. Remote Sens. Lett.*, vol. 13, no. 11, pp. 1651–1655, Nov. 2016.

[7] S. Wang and X. C. Zhang, "Pulsed terahertz tomography," *J. Phys. D, Appl. Phys.*, vol. 37, no. 6, p. 964, Mar. 2004.

[8] X. Zhang, Q. Guo, T. Chang, and H.-L. Cui, "Broadband stepped-frequency modulated continuous terahertz wave tomography for non-destructive inspection of polymer materials," *Polym. Test.*, vol. 76, pp. 455–463, Jul. 2019.

[9] J. Gao, Y. Qin, B. Deng, H. Wang, and X. Li, "A novel method for 3-D millimeter-wave holographic reconstruction based on frequency interferometry techniques," *IEEE Trans. Microw. Theory Techn.*, vol. 66, no. 3, pp. 1579–1596, Mar. 2018.

[10] L. M. Sim, T. C. Tan, A. A. Mon, and B. S. Wong, "X-ray absorption-based technique to measure the thickness of multi-layered structures," *NDT E Int.*, vol. 42, no. 4, pp. 291–296, Jun. 2009.

[11] C.-W. You, C. Lu, T.-Y. Wang, S.-R. Qian, Z.-G. Yang, K.-J. Wang, J.-S. Liu, and S.-L. Wang, "Method for defect contour extraction in terahertz non-destructive testing conducted with a raster-scan THz imaging system," *Appl. Opt.*, vol. 57, no. 17, pp. 4884–4889, Jun. 2018.

[12] J. Gao, Z. Cui, B. Cheng, Y. Qin, X. Deng, B. Deng, X. Li, and H. Wang, "Fast three-dimensional image reconstruction of a standoff screening system in the terahertz regime," *IEEE Trans. THz Sci. Technol.*, vol. 8, no. 1, pp. 38–51, Jan. 2018.

[13] E. Brundermann, M. Havenith, G. Scalari, M. Giovannini, J. Faist, J. Kunsch, L. Mechold, and M. Abraham, "Turn-key compact high temperature terahertz quantum cascade lasers: Imaging and room temperature detection," *Opt. Express*, vol. 14, no. 5, pp. 1829–1841, Mar. 2006.

[14] D. Crawley, S. Withington, and J. Obradovic, "Area-scan camera for terahertz holography," *Rev. Sci. Instrum.*, vol. 77, no. 5, May 2006, Art. no. 053106.

[15] H. Huang, P. Qiu, S. Panezai, S. Hao, D. Zhang, Y. Yang, Y. Ma, H. Gao, L. Gao, Z. Zhang, and Z. Zheng, "Continuous-wave terahertz high-resolution imaging via synthetic hologram extrapolation method using pyroelectric detector," *Opt. Laser Technol.*, vol. 120, Dec. 2019, Art. no. 105683.

[16] W. L. Chan, J. Deibel, and D. M. Mittleman, "Imaging with terahertz radiation," *Rep. Progr. Phys.*, vol. 70, no. 8, pp. 1325–1379, Jul. 2007.

[17] C. Janke, M. Först, M. Nagel, H. Kurz, and A. Bartels, "Asynchronous optical sampling for high-speed characterization of integrated resonant terahertz sensors," *Opt. Lett.*, vol. 30, no. 11, pp. 1405–1407, 2005.

[18] T. Chang, X. Zhang, X. Zhang, and H.-L. Cui, "Accurate determination of dielectric permittivity of polymers from 75 GHz to 1.6 THz using both S-parameters and transmission spectroscopy," *Appl. Opt.*, vol. 56, no. 12, pp. 3287–3292, Apr. 2017.

[19] K. B. Cooper, R. J. Dengler, N. Llombart, B. Thomas, G. Chattopadhyay, and P. H. Siegel, "THz imaging radar for standoff personnel screening," *IEEE Trans. THz Sci. Technol.*, vol. 1, no. 1, pp. 169–182, Sep. 2011.

[20] A.-A.-A. Boulogeorgos, A. Alexiou, T. Merkle, C. Schubert, R. Elschner, A. Katsiotis, P. Stavrianos, D. Kritharidis, P.-K. Chartsias, J. Kokkoniemi, M. Juntti, J. Lehtomaki, A. Teixeira, and F. Rodrigues, "Terahertz technologies to deliver optical network quality of experience in wireless systems beyond 5G," *IEEE Commun. Mag.*, vol. 56, no. 6, pp. 144–151, Jun. 2018.

[21] H.-M. Chen, S. Lee, R. M. Rao, M.-A. Slamani, and P. K. Varshney, "Imaging for concealed weapon detection: A tutorial overview of development in imaging sensors and processing," *IEEE Signal Process. Mag.*, vol. 22, no. 2, pp. 52–61, Mar. 2005.

[22] L. Li, J. Yang, G. Cui, Z. Jiang, and X. Zheng, "Method of passive MMW image detection and identification for close target," *J. Infr., Millim., THz Waves*, vol. 32, no. 1, pp. 102–115, Jan. 2011.

[23] K. B. Cooper, R. J. Dengler, G. Chattopadhyay, E. Schlecht, J. Gill, A. Skalare, I. Mehdi, and P. H. Siegel, "A high-resolution imaging radar at 580 GHz," *IEEE Microw. Wireless Compon. Lett.*, vol. 18, no. 1, pp. 64–66, Jan. 2008.

[24] K. B. Cooper, R. J. Dengler, N. Llombart, T. Bryllert, G. Chattopadhyay, E. Schlecht, J. Gill, C. Lee, A. Skalare, I. Mehdi, and P. H. Siegel, "Penetrating 3-D imaging at 4- and 25-m range using a submillimeter-wave radar," *IEEE Trans. Microw. Theory Techn.*, vol. 56, no. 12, pp. 2771–2778, Dec. 2008.

[25] B. Blazquez, K. B. Cooper, and N. Llombart, "Time-delay multiplexing with linear arrays of THz radar transceivers," *IEEE Trans. THz Sci. Technol.*, vol. 4, no. 2, pp. 232–239, Mar. 2014.

[26] K. B. Cooper, S. Durden, M. Choukroun, M. Lebsock, J. Siles, R. Monje, and C. Lee, "FMCW radars at 95 and 183 GHz for planetary and Earth science remote sensing," presented at the Global Symp. Millim. Waves, Espoo, Finland, Jun. 6-8, 2016.

[27] D. M. Sheen, T. E. Hall, R. H. Severtsen, D. L. McMakin, B. K. Hatchell, and P. L. J. Valdez, "Active wideband 350 GHz imaging system for concealed-weapon detection," presented at the Passive Millim.-Wave Imag. Technol. XII, Orlando, FL, USA, 2009.

[28] D. M. Sheen, T. E. Hall, R. H. Severtsen, D. L. McMakin, B. K. Hatchell, and P. L. J. Valdez, "Standoff concealed weapon detection using a 350 GHz radar imaging system," presented at the Passive Millim.-Wave Imag. Technol. XIII, Orlando, Florida, USA, 2009.

[29] D. M. Sheen, "Sparse multi-static arrays for near-field millimeter-wave imaging," presented at the 1st IEEE Global Conf. Signal Inf. Process., TX, USA, Dec. 3-5, 2013.

[30] D. M. Sheen and T. E. Hall, "Reconstruction techniques for sparse multi-static linear array microwave imaging," presented at the Conf. Passive Active Millim.-Wave Imag. XVII, Baltimore, MD, USA, May 8-9, 2014.

[31] M. Caris, S. Stanko, A. Wahlen, R. Sommer, J. Wilcke, N. Pohl, A. Leuther, and A. Tessmann, "Very high resolution radar at 300 GHz," presented at the 11th Eur. Radar Conf., Rome, Italy, Oct. 8-10, 2014.

[32] H. Essen, S. Stanko, R. Sommer, A. Wahlen, R. Brauns, J. Wilcke, W. Johannes, A. Tessmann, and M. Schlechtweg, "A high performance 220-GHz broadband experimental radar," presented at the 33rd Int. Conf. Infr., Pasadena, CA, USA, Sep. 15-19, 2008.

[33] H. Essen, A. Wahlen, R. Sommer, G. Konrad, M. Schlechtweg, and A. Tessmann, "Very high bandwidth millimetre-wave radar," *Electron. Lett.*, vol. 41, no. 22, pp. 1247–1249, Oct. 2005.

[34] C. A. Weg, W. von Spiegel, R. Henneberger, R. Zimmermann, T. Loeffler, and H. G. Roskos, "Fast active THz cameras with ranging capabilities," *J. Infr., Millim., THz Waves*, vol. 30, no. 12, pp. 1281–1296, Aug. 2009.

[35] N. S. Schreiner, W. Sauer-Greff, R. Urbansky, G. von Freymann, and F. Friederich, "Multilayer thickness measurements below the Rayleigh limit using FMCW millimeter and terahertz waves," *Sensors*, vol. 19, no. 18, p. 3910, Sep. 2019.

[36] E. Cristofani, F. Friederich, S. Wohnsiedler, C. Matheis, J. Jonuscheit, M. Vandewal, and R. Beigang, "Nondestructive testing potential evaluation of a terahertz frequency-modulated continuous-wave imager for composite materials inspection," *Opt. Eng.*, vol. 53, no. 3, Mar. 2014, Art. no. 031211.
[37] M. Abbasi, S. E. Gunnarsson, N. Wadefalk, R. Kozhuharov, J. Svedin, S. Cherednichenko, I. Angelov, I. Kallfass, A. Leuther, and H. Zirath, "Single-chip 220-GHz active heterodyne receiver and transmitter MMICs with on-chip integrated antenna," *IEEE Trans. Microw. Theory Techn.*, vol. 59, no. 2, pp. 466–478, Feb. 2011.
[38] R. Dahlback, T. Rubaek, T. Bryllert, M. Persson, and J. Stake, "A 340 GHz CW non-linear imaging system," presented at the 35th Int. Conf. Infr., Millim., THz Waves, Rome, Italy, Sep. 5-10, 2010.
[39] D. A. Robertson, P. N. Marsh, D. R. Bolton, R. J. C. Middleton, R. I. Hunter, P. J. Speirs, D. G. Macfarlane, S. L. Cassidy, and G. M. Smith, "340 GHz 3D radar imaging test bed with 10 Hz frame rate," presented at the Passive Act. Millim.-Wave Imag. XV, Baltimore, MD, USA, Apr. 26, 2012.
[40] B. Mencia-Oliva, J. Grajal, and A. Badolato, "100-GHz FMCW radar front-end for ISAR and 3D imaging," presented at the IEEE Nat. Radar Conf., Kansas City, MI, USA, May 23-27, 2011.
[41] S. Chen, C. Luo, B. Deng, H. Wang, Y. Cheng, and Z. Zhuang, "Three-dimensional terahertz coded-aperture imaging based on single input multiple output technology," *Sensors*, vol. 18, no. 1, p. 303, Jan. 2018.
[42] G. Dai, G. Geng, X. Zhang, J. Wang, T. Chang, and H.-L. Cui, "W-band near-field microscope," *IEEE Access*, vol. 7, pp. 48060–48067, 2019.
[43] H.-B. Liu, H. Zhong, N. Karpowicz, Y. Chen, and X.-C. Zhang, "Terahertz spectroscopy and imaging for defense and security applications," *Proc. IEEE*, vol. 95, no. 8, pp. 1514–1527, Aug. 2007.
[44] J.-B. Yan, D. Gomez-Garcia Alvestegui, J. W. McDaniel, Y. Li, S. Gogineni, F. Rodriguez-Morales, J. Brozena, and C. J. Leuschen, "Ultrawideband FMCW radar for airborne measurements of snow over sea ice and land," *IEEE Trans. Geosci. Remote Sens.*, vol. 55, no. 2, pp. 834–843, Feb. 2017.
[45] I. Jaeger, L. Zhang, J. Stiens, H. Sahli, and R. Vounckx, "Millimeter wave inspection of concealed objects," *Microw. Opt. Technol. Lett.*, vol. 49, no. 11, pp. 2733–2737, Nov. 2007.
[46] X. Zhang, J. Liang, N. Wang, T. Chang, Q. Guo, and H.-L. Cui, "Broadband millimeter-wave imaging radar-based 3-D holographic reconstruction for nondestructive testing," *IEEE Trans. Microw. Theory Techn.*, vol. 68, no. 3, pp. 1074–1085, Mar. 2020.
[47] J. Luo, Z. Xie, and M. Xie, "Frequency estimation of the weighted real tones or resolved multiple tones by iterative interpolation DFT algorithm," *Digit. Signal Process.*, vol. 41, pp. 118–129, Jun. 2015.
[48] J. Luo and M. Xie, "Phase difference methods based on asymmetric windows," *Mech. Syst. Signal Process.*, vols. 54–55, pp. 52–67, Mar. 2015.
[49] D. Belega, D. Dallet, and D. Petri, "Accuracy of the normalized frequency estimation of a discrete-time sine-wave by the energy-based method," *IEEE Trans. Instrum. Meas.*, vol. 61, no. 1, pp. 111–121, Jan. 2012.
[50] A. V. Prabhu, V. K. Aatre, T. Soumini, and S. A. Karipel, "Frequency zooming techniques for high resolution spectrum analysis," *Defence Sci. J.*, vol. 35, no. 3, pp. 281–285, Jan. 1985.
[51] L. R. Rabiner, R. W. Schafer, and C. M. Rader, "The chirp z-transform algorithm and its application," *Bell Syst. Tech. J.*, vol. 48, no. 5, pp. 1249–1292, May 1969.
[52] W. Liao, "MUSIC for multidimensional spectral estimation: Stability and super-resolution," *IEEE Trans. Signal Process.*, vol. 63, no. 23, pp. 6395–6406, Dec. 2015.
[53] R. Ray and T. Kailath, "ESPRIT—Estimation of signal parameters via rotational invariance techniques," *Opt. Eng.*, vol. 29, no. 4, pp. 296–313, Apr. 1990.
[54] L. Tsang, J. A. Kong, K.-H. Ding, *Scattering of Electromagnetic Waves: Theories and Applications*. New York, NY, USA: Wiley, 2000, pp. 54–60.
[55] S. Nojavan and F.-G. Yuan, "Damage identification using electromagnetic waves based on born imaging algorithm," *J. Eng. Mech.*, vol. 135, no. 7, pp. 717–728, Jul. 2009.
[56] Q. Guo, T. Chang, G. Geng, C. Jia, and H.-L. Cui, "A high precision terahertz wave image reconstruction algorithm," *Sensors*, vol. 16, no. 7, p. 1139, Jul. 2016.
[57] J. M. Lopez-Sahcnez and J. Fortuny-Guasch, "3-D radar imaging using range migration techniques," *IEEE Trans. Antennas Propag.*, vol. 48, no. 5, pp. 728–737, May 2000.
[58] S. Gu, C. Li, X. Gao, Z. Sun, and G. Fang, "Three-dimensional image reconstruction of targets under the illumination of terahertz Gaussian beam—Theory and experiment," *IEEE Trans. Geosci. Remote Sens.*, vol. 51, no. 4, pp. 2241–2249, Apr. 2013.
[59] Z. Sun, C. Li, S. Gu, and G. Fang, "Fast three-dimensional image reconstruction of targets under the illumination of terahertz Gaussian beams with enhanced phase-shift migration to improve computation efficiency," *IEEE Trans. THz Sci. Technol.*, vol. 4, no. 4, pp. 479–489, Jul. 2014.
[60] R. Zhu, J. Zhou, G. Jiang, and Q. Fu, "Range migration algorithm for near-field MIMO-SAR imaging," *IEEE Geosci. Remote Sens. Lett.*, vol. 14, no. 12, pp. 2280–2284, Dec. 2017.
[61] W. Zhang, A. Hoorfar, and C. Thajudeen, "Two- and three-dimensional fast intrawall imaging with microwave tomographic algorithm," *Int. J. Antennas Propag.*, vol. 2018, Jan. 2018, Art. no. 7267601.
[62] W. E. Sabin, *Discrete-Signal Analysis and Design*. Hoboken, NJ, USA: Wiley, 2008, pp. 129–151.

XIAOXUAN ZHANG received the B.S. degree from the School of Electro-Mechanical Engineering, Qingdao University, in 2015, and the Ph.D. degree from the College of Instrumentation and Electrical Engineering, Jilin University, in 2020. Her research interests include three-dimensional terahertz tomographic imaging radar and non-destructive detection of defects in composite materials.

TIANYING CHANG received the Ph.D. degree from the College of Control Science and Engineering, Shandong University, in 2009. From 2007 to 2008, she was a Joint Ph.D. Student with the Stevens Institute of Technology. She was a Lecturer with Shandong University. She was also a Postdoctoral Research Associate with New York University. She is currently an Associate Professor with Jilin University. Her research interests include optical fiber sensor, THz systems, and nano-optics.

ZHONGMIN WANG received the B.S. degree in automation from the School of Electrical Engineering, University of Jinan, Jinan, China, in 2005, and the M.S. degree in control theory and control engineering from the College of Control Science and Engineering, Shandong University, Jinan, in 2008. He is currently pursuing the Ph.D. degree with the College of Instrumentation and Electrical Engineering, Jilin University, Changchun, China. From 2009 to 2016, he was an Assistant Researcher with the Shandong Academy of Sciences, China. His research interests include millimetre-wave imaging and optical fiber sensors.

HONG-LIANG CUI received the Ph.D. degree in theoretical physics from the Stevens Institute of Technology, in 1987. He was a Professor of physics and engineering physics with the Stevens Institute of Technology, and a Professor of applied physics with New York University. He is currently a Professor of electrical engineering with Jilin University. His research interests include solid-state electronics, fiber optical communication and sensing, high-frequency electromagnetic wave propagation and interaction with matter, physics-based approaches to modeling of semiconductor, and molecular devices.